

Wet Imprinting of Channel-Type Superstructures in Nanostructured Titania Thin Films at Low Temperatures for Hybrid Solar Cells

Lin Song,^[a] Tianyi Wang,^[a, e] Volker Körstgens,^[a] Weijia Wang,^[b] Nitin Saxena,^[a] Christoph J. Schaffer,^[a] Thomas Fröschl,^[c] Nicola Hüsing,^[c] Sigrid Bernstorff,^[d] and Peter Müller-Buschbaum^{*[a]}

Hierarchically structured titania films, exhibiting interconnected foam-like nanostructures and large-scale channel-type superstructures, were achieved in an energy-saving way at low temperatures by a polymer template-assisted sol-gel synthesis in combination with a wet-imprinting process. The surface morphology was probed with scanning electron microscopy and atomic force microscopy, whereas the inner morphology was characterized with grazing incidence small-angle X-ray scattering measurements. Compared to the initial hybrid films, the titania films showed reduced structure sizes caused by removal of the polymer template. UV/Vis measurements showed an additional light-scattering effect at various angles of light inci-

dence in the hierarchically structured titania films, which resulted in higher light absorption in the wet-imprinted active layer. To give proof of viability, the titania films were evaluated as photoanodes for dye-free hybrid solar cells. The dye-free layout allowed for low-cost fabrication, avoided problems related to dye bleaching, and was a more environmentally friendly alternative to using dyes. Under different angles of light incidence, the enhancement in the short-circuit current density was in good agreement with the improvement in light absorption in the superstructured active layer, demonstrating a positive impact of the superstructures on the photovoltaic performance of hybrid solar cells.

Introduction

Dye-free hybrid solar cells based on n-type titania thin films and p-type polymers such as poly(3-hexylthiophene) (P3HT) are of research interest owing to the possibility of combining

the merits of both the inorganic and organic components.^[1–4] Among the advantages, it can be highlighted that titania provides hybrid devices with high stability of the active layer morphology and allows for low-cost fabrication; in addition, titania is nontoxic and has a widely tunable morphology.^[5–7] The p-type polymers are lightweight, have facile solution processability, and allow the possibility to make flexible devices.^[8–10] Despite these advantages, major problems regarding the achievable power conversion efficiency (PCE) still need to be solved. However, with continuous progress and development, hybrid solar cells can become highly attractive as next-generation-type solar cells. For example, Lin et al. demonstrated an improved performance of P3HT:TiO₂ hybrid solar cells by covalently bonding silica nanodots to the hole-transport layer.^[11] Mattioli et al. applied an intercalated layer into the P3HT:ZnO active layer to achieve a ternary hybrid heterojunction that enhanced solar-cell efficiency.^[12] Ben Dkhil et al. modified ZnO photoanodes with a p-type semiconductor surfactant to increase the photovoltaic performance of hybrid devices.^[13] Beyond chemical tuning, the design of the optical properties of hybrid solar cells has been proposed to enhance light harvesting thereby to improve device performance. It was reported that light management could be improved by introducing hierarchical structures in the active layers of solar cells by combining nanostructures with larger scale structures.^[14–16] For example, Niedermeier et al. demonstrated an increased absorbance of visible light in titania films that combined macrochan-

[a] Dr. L. Song, T. Wang, Dr. V. Körstgens, N. Saxena, Dr. C. J. Schaffer, Prof. Dr. P. Müller-Buschbaum
Lehrstuhl für Funktionelle Materialien
Physik-Department
Technische Universität München
James-Franck-Str. 1, 85748 Garching (Germany)
E-mail: muellerb@ph.tum.de

[b] Dr. W. Wang
State Key Laboratory of Solidification Processing
School of Materials Science and Engineering
Northwestern Polytechnical University
Youyixilu 127, Xi'an 710072 (PR China)

[c] T. Fröschl, Prof. Dr. N. Hüsing
Materialchemie, Chemie und Physik der Materialien
Universität Salzburg
Jakob-Haringer Str. 2a, 5020 Salzburg (Austria)

[d] Dr. S. Bernstorff
Elettra-Sincrotrone Trieste S.C.p.A.
Strada Statale 14–km 163.5 in AREA Science Park Basovizza, 34149 Trieste (Italy)

[e] T. Wang
Center for Nanophotonics
AMOLF
Science Park 104, 1098 XG Amsterdam (The Netherlands)

Supporting Information and the ORCID identification number(s) for the author(s) of this article can be found under <https://doi.org/10.1002/cssc.201800129>.

neled superstructures and mesoporous nanostructures.^[14] Chou et al. produced hierarchically structured ZnO films with primary nanoparticles and secondary colloidal spheres and found an enhancement in the short-circuit current density in superstructured dye-sensitized solar cells (DSSCs).^[15] Shih et al. fabricated hill-like hierarchical structures of TiO₂ photoanodes to increase light scattering and dye loading, which improved the photovoltaic performance.^[16] To introduce large-scale superstructures in nanostructured films, the imprinting technique, involving the use of relief-featured molds to deform the imprinted materials mechanically, is a common approach, as it is facile and cost effective. In particular, nanoimprint lithography (NIL) has been used in photovoltaic applications to control the length scale of the donor–acceptor phase separation structure thereby to promote charge separation and transport.^[17–19] This technique allows short imprinting times, high throughput and resolution, low energy input, and ease of processing. However, NIL requires special machinery that is capable of providing high pressures, especially for the imprinting of hard materials. As an inexpensive alternative, the wet-imprinting process, also sometimes referred to as solution-based micromolding in capillaries (MiMiC), can achieve superstructures under ambient conditions without the requirement of special machinery.^[20–23] Poly(dimethylsiloxane) (PDMS) is typically selected as the mold material for wet imprinting. Wet imprinting with a PDMS mold has been successfully applied in structuring a broad range of materials, including polymers,^[20,21] metal oxides,^[22,23] and organic–inorganic composite materials.^[14] On the one hand, PDMS is elastomeric, which allows for conformal contact with the substrate to replicate faithfully the existing relief features. On the other hand, PDMS has a relatively low interfacial free energy, which is beneficial for the lift-off process after imprinting.^[24] Owing to capillary forces, the solution of the imprinted material fills the large-scale structures of the PDMS mold efficiently. Once the solvent evaporates completely, the PDMS mold can be lifted off from the support.

Mesoporous titania films have been widely studied in photovoltaic applications, and the performance of photovoltaic devices is closely related to the extent and nature of the crystalline titania phase.^[25–27] Usually, calcination above 400 °C is an efficient way to obtain crystalline titania and also to achieve mesopores inside the titania by combusting the polymer template.^[28–30] However, the need for high-temperature processing excludes the possibility to use flexible polymer substrates such as polyethylene terephthalate (PET) and polyethylene naphthalate (PEN) foils, as they are typically not heat resistant. To access lightweight and flexible devices, fabricating mesoporous titania films in crystalline form at low temperatures is of high interest.^[31–34] Moreover, a low-temperature synthesis reduces the energy necessary for device fabrication, which results in lower production costs and, in turn, shorter pay-back times of these solar cells in combination with a lower impact on the environment. Therefore, hybrid solar cells with rigid substrates will also benefit from reduced fabrication temperatures, that is, avoiding calcination at temperatures above 400 °C.

Previously, we demonstrated the use of NIL to introduce square pitch-like lattice superstructures in mesoporous titania films, which led to an enhancement in light absorption. The superstructured active layer enabled better photovoltaic performance.^[31] In the present work, we pick up the idea of low-temperature processing to realize superstructured titania films for use in hybrid solar cells. We target one-dimensional grating channels established by wet imprinting, replacing the square pitch-like lattice superstructures studied before. We prepare mesoporous titania films with a foam-like morphology by sol-gel chemistry in combination with the diblock copolymer polystyrene-*block*-polyethylene oxide (PS-*b*-PEO) acting as structure-directing agent. The so-called block-copolymer-assisted sol-gel synthesis allows tuning of the morphology of the titania films with structures ranging from nanogranules to nanoscale vesicles.^[28,35–37] In particular, foam-like nanostructures exhibiting an interconnected network are desirable in photovoltaic applications, as they can provide a high surface-to-volume ratio and continuous paths for charge-carrier transport.^[30,38,39] A special titania precursor, ethylene glycol modified titanate (EGMT), imparts crystallinity upon the sol-gel-derived titania.^[34,40,41] Additionally, the crystalline phase of titania can be efficiently tuned by increasing the pH value in the sol-gel process from the rutile to anatase phase.^[42,43] Channeled superstructures of a one-dimensional grating type are produced by wet imprinting. In combination with the mesoporous titania films, hierarchically structured films are achieved. Scanning electron microscopy (SEM) and atomic force microscopy (AFM) measurements reveal length scales at the surface of the hierarchically structured titania films. The information about nanostructure and mesopore size inside the films is provided by grazing incidence small-angle X-ray scattering (GISAXS) measurements. The optoelectronic properties and current–voltage (*J*–*V*) characteristics are compared in the low-temperature processed hybrid solar cells with and without channel-type superstructures.

Results and Discussion

Fabrication of superstructures and nanostructures

The manufacturing process of hierarchically structured titania films is schematically illustrated in Figure 1.

First, the block-copolymer-assisted sol-gel synthesis is applied to prepare mesoporous titania films with a foam-like nanoscale morphology. Owing to the presence of a so-called good–poor solvent pair (DMF is a good solvent and HCl is a poor solvent in this work), the self-assembly behavior drives the diblock copolymer to form so-called crew-cut micelles with PS cores and PEO coronas. In addition, titania species are attached to the PEO domains through the formation of coordination bonds during the sol-gel process, as shown in Figure 1 a. After the sol-gel process, the solution is spin coated to remove most of the solvents and to obtain titania:PS-*b*-PEO composite films (Figure 1 b, c). Afterwards, a droplet of the sol-gel solution is put at the edge of the PDMS mold, and then the obtained titania:PS-*b*-PEO composite film is used as a sup-

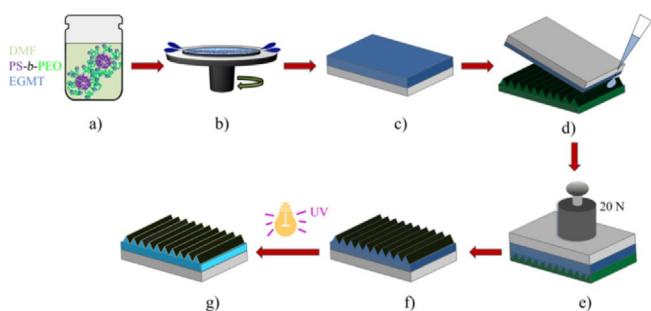


Figure 1. Illustration of the wet-imprinting process: a) polymer-template-assisted sol-gel chemistry, b) spin coating of the prepared solution, c) obtained titania:PS-*b*-PEO composite film, d) covering the composite film on a PDMS mold after placing a drop of sol-gel solution on one end of the mold, e) embossing of the titania:PS-*b*-PEO composite film at a pressure of 20 N, f) wet-imprinted titania:PS-*b*-PEO composite film after mold lift-off, g) mesoporous titania film with one-dimensional grating channels after UV exposure and presoaking process.

port to be placed down to cover the drop (Figure 1d). The channels in the PDMS mold are filled spontaneously with the sol-gel solution by capillary action. Then, a low force of 20 N is applied on top of the support, as shown in Figure 1e. After total evaporation of the solvents, the PDMS mold is removed from the support to obtain the superstructured titania:PS-*b*-PEO composite film (Figure 1f). This process transfers negative replicas of the patterns on the PDMS mold to the imprinted material. In the end, UV irradiation and a presoaking process are chosen to remove the polymer template and achieve mesoporous titania films with 1D channelled superstructures (Figure 1g).

Figure 2a shows an optical micrograph of a titania:PS-*b*-PEO composite film after wet imprinting. The sample exhibits ordered channel-like structures, which suggests homogeneous transfer of the structures on the mold over a macroscopic area. The superstructures are displayed with SEM at different magnifications in Figure 2b,c. The channel-grating structures have a periodicity of 1.35 μm with channel and valley widths of

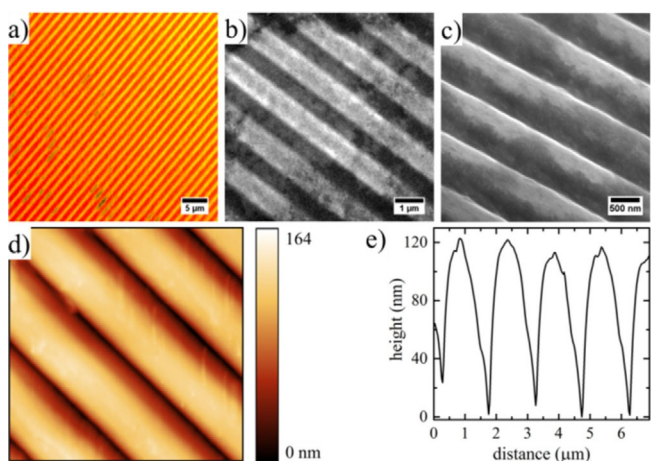


Figure 2. a) Optical microscopy and b) plane-view SEM images of the wet-imprinted titania:PS-*b*-PEO composite film. c) SEM image of the film measured at a tilt angle of 54°. d) AFM topography of the film (scan range 5 \times 5 μm^2) and e) its corresponding height profile.

0.80 μm and 0.55 μm , respectively. For better vision of the superstructures, the sample was tilted with respect to the electron beam during the SEM measurements. The transverse section of the channels is nonrectangular (Figure 2c), which is different from other macrochannels reported in the literature having a rectangular shape.^[14,20] AFM measurements confirm the ordered array of the channelled superstructures with a periodicity of 1.35 μm (Figure 2d). The height profile reveals that the average channel height is approximately 120 nm and confirms the arch shape (Figure 2e). After the wet-imprinting process, the PS-*b*-PEO template is extracted from the superstructured composite film to obtain the nanostructured titania network. The resulting surface morphology was mapped with SEM and AFM, as shown in Figure 3.

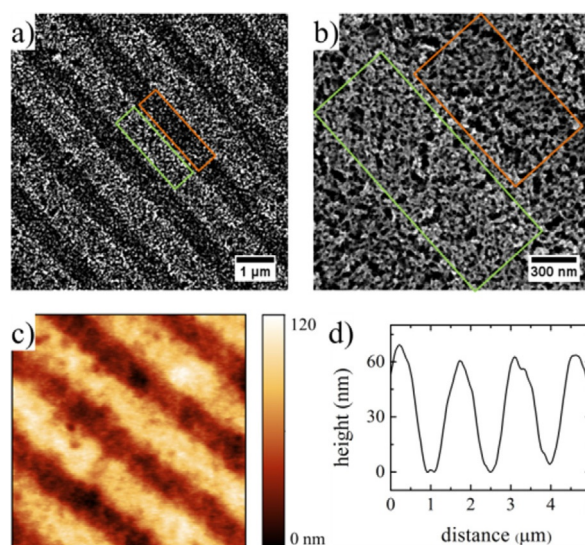


Figure 3. a) Low-magnification and b) high-magnification SEM images of wet-imprinted titania films with foam-like morphology after polymer-template removal from the composite film. Green and red rectangles mark the channelled superstructure and the valley between the superstructures, respectively. c) AFM topography of the hierarchically structured film (scan range 5 \times 5 μm^2) and d) its corresponding height profile.

After polymer-template extraction, the channelled superstructures are preserved with similar channel and valley widths but with an increase in the surface roughness, as compared to the composite films (Figure 3a). Titania nanostructures and mesopores are pictured with SEM at a higher magnification in Figure 3b. The mesoporous nature of the foam-like titania morphology is observed on both the channel and valley, displaying a bicontinuous titania network on the nanoscale. Moreover, image grain analysis reveals mesopore sizes within 10–20 nm. This size range in combination with the titania nanostructures appears promising for the desired photovoltaic applications^[44,45] but could also be of interest for photocatalysis^[46] and Li-ion batteries.^[47,48] The AFM measurements confirm the preserved channel-like superstructures (Figure 3c) with an average height of approximately 60 nm (Figure 3d). Thus, compared to the superstructures before polymer extraction, the channel height is reduced by approximately 50%. A similar ob-

ervation was reported by Guldin et al., who demonstrated that titania:PI-*b*-PEO composite films underwent shrinkage of the film thickness over 50% after polymer extraction.^[29] This reduction is ascribed to the collapse of the titania nanostructures induced by removal of the polymer scaffold and condensation of TiOH to TiO₂.^[29]

To gain a view of the inner film morphology, the wet-imprinted titania:PS-*b*-PEO composite films were probed with GISAXS measurements before and after polymer extraction. GISAXS offers high statistics about the domain-size distribution and spatial arrangement with a resolution ranging from the nanoscale to the mesoscale in a thin-film geometry.^[49–51] The 2D GISAXS data of both films are displayed in Figure S1 (Supporting Information) with a detailed feature description in the Supporting Information. To obtain information about lateral structures in the film, horizontal line cuts were performed for both samples at the Yoneda peak position. This peak is the maximum of the diffuse scattering, which is material characteristic and is located at the critical angle of the probed material.^[52] For the sample before polymer extraction, titania species are covalently embedded in the PEO matrix, and the scattering length density of the mixture of titania and PEO is higher than that of pure PS domains, giving contrast to the system. Therefore, the Yoneda peak position of the titania:PEO mixture was chosen for the horizontal line cut, which is plotted in Figure 4a.

To gain quantitative information about domain sizes and spatial correlations of the titania:PS-*b*-PEO composite film, the horizontal line cut was fitted within the framework of the distorted wave Born approximation (DWBA),^[53,54] assuming two form factors with cylindrical geometry distributed over a 1D paracrystal lattice.^[55,56] From data modeling, the obtained information about characteristic structures describes the inner morphology. The domain radii of the titania:PEO composites of

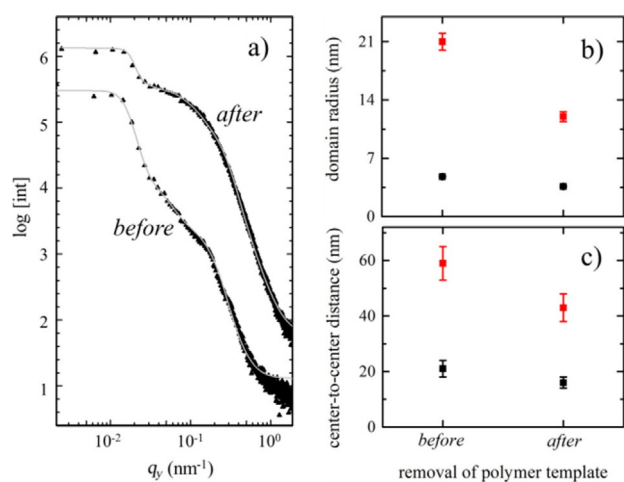


Figure 4. a) Horizontal line cuts of the 2D GISAXS data for the hierarchically structured titania films. The bottom and top black curves were measured at the film before and after removal of the polymer template. The gray lines represent the fits to the data. All curves are shifted along the intensity axis for clarity of presentation. Extracted characteristic length scales are b) domain radii and c) domain center-to-center distances. Black and red squares indicate small-sized and large-sized domains, respectively.

(4.8 ± 0.1) and (21.0 ± 1.1) nm with their corresponding center-to-center distances of (21 ± 3) and (59 ± 5) nm are found before polymer extraction (Figure 4b,c). For the film after polymer extraction, only titania remains. The fitting model is the same as for the sample before polymer extraction. Characteristic domain radii of (3.6 ± 0.1) and (12.0 ± 0.6) nm with center-to-center distances of (16 ± 3) and (43 ± 5) nm are observed for the titania nanostructures (Figure 4b,c), and the mesopore sizes are calculated to be (9 ± 3) and (19 ± 5) nm following the model introduced in our previous work.^[7,31]

From this analysis of the samples before and after polymer extraction, it can be concluded that both domain sizes of the titania nanostructures are smaller than those of the titania:PEO composite. This shrinkage is ascribed to collapse of the titania nanostructures induced by removal of the polymer scaffold.^[8,37,57,58] Moreover, the polymer-extraction process enables interconnection of the nanostructured titania to form a network, which allows transport of charge carriers to the electrode in the hybrid solar cells. After polymer extraction, mesopores and nanostructures are present inside the titania films, which is in line with the observation of the sample surface. In general, the mesoporous nature is preserved in the wet-imprinted titania films.

Optical properties of hierarchical structured films

The UV/Vis absorption spectra of the mesoporous titania films with and without wet imprinting were compared at various angles of light incidence, as shown in Figure 5a. The hierarchi-

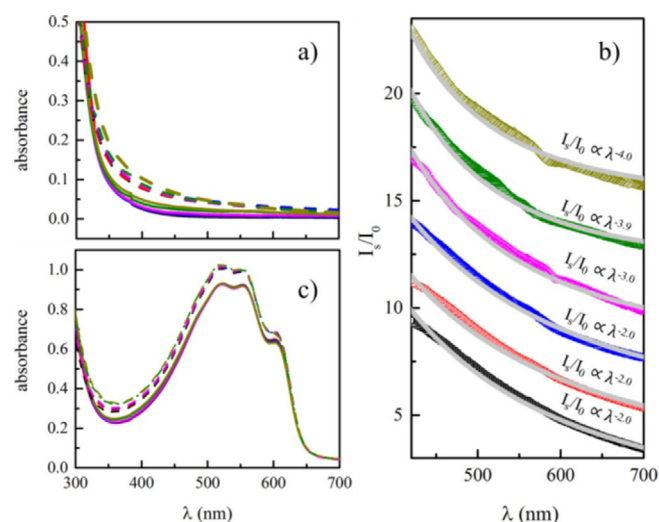


Figure 5. a) UV/Vis absorption spectra of a planar titania film (solid lines) and a wet-imprinted film (dashed lines) under various angles of light incidence. Black, red, blue, pink, green, and yellow curves represent UV/Vis measurements at incident angles of 0, 10, 20, 30, 40, and 50°, respectively. b) Light-scattering spectra of the wet-imprinted titania film over the wavelength range of 400 to 700 nm. The gray lines represent the fits (power function) to the data. All curves are shifted along the intensity axis for clarity of presentation. c) UV/Vis absorption spectra of a planar active layer (solid lines) and a wet-imprinted active layer (dashed lines) under various angles of light incidence.

cal structures can influence the light absorption of the films, as reported in the literature.^[15–17,59]

An increased angular-dependent absorbance was observed in the wet-imprinted film over almost the full investigated wavelength range as compared to the titania film without superstructures, denoted as the planar film. This additional absorption is due to light scattering induced by the presence of channeled superstructures. Furthermore, the angular-dependent scattering intensities of the wet-imprinted sample were fitted with power functions over the wavelength range of 400 to 700 nm (Figure 5b), as visible light is mainly utilized for solar-cell applications. From the fitting, we observe that I_s/I_0 is proportional to λ^{-2} at incident angles of 0, 10, and 20°, whereas it is proportional to λ^{-3} at a 30° incident angle and to λ^{-4} at incident angles of 40 and 50°. Here, λ is the wavelength, I_s and I_0 are the intensities of scattered and incident light, respectively. Thus, at incident angles of 40 and 50°, Rayleigh scattering is found, which suggests that the height of the superstructures dominates the light scattering, as the superstructure length and periodicity are larger than the wavelength of visible light. Moreover, the exponents of λ decrease from -2 to -4 , which indicates Rayleigh scattering becomes dominant in the channel-superstructured film with increasing incident angles. Figure 5c shows the angular-dependent absorption spectra of the active layer that was prepared by backfilling P3HT into the mesoporous titania films. Both hierarchical and planar active layers show a similar absorption shape at different angles of light incidence, implying that no significant change in the optical properties is observed by superstructuring titania photoanodes and by measuring at different angles. However, it can be seen that at all angles of light incidence the wet-imprinted active layer harvests more light than the planar active layer over the wavelength range of visible light, which is ascribed to the existence of additional light-scattering centers in the wet-imprinted active layer. In detail, by integrating the light absorption over the wavelength range of 400 to 700 nm, light-absorption enhancements of 10.6, 10.9, 11.2, 11.8, 12.1, and 12.0% are found in the wet-imprinted active layer as compared to the planar active layer at incident angles of 0, 10, 20, 30, 40, and 50°. These similar values suggest that the light-absorption enhancement is not influenced by the different types of light scattering in the superstructured titania film at various angles of light incidence. This behavior is different from the observation in our previous study, in which we demonstrated an increase in light absorption upon increasing the measuring

angles in the active layer with a square pitch-like lattice superstructure.^[31] The absence of angular dependence appears beneficial for real-world applications, as such solar cells could be used at many different places without the need for optimization of the angular alignment.

Current–voltage characteristics

The hierarchically structured titania films were used as photoanodes for dye-free hybrid solar cells to give proof of viability. For comparison, hybrid solar cells with planar titania photoanodes were also fabricated. To link with the optical properties discussed above, both types of hybrid solar cells were also measured at different angles of light incidence.

Figure 6a exemplarily compares the current–voltage (J – V) characteristics of both solar cells under standard conditions (at 0° incident angle). The planar hybrid solar cells have a PCE of $(0.11 \pm 0.01)\%$ with an open-circuit voltage (V_{oc}) of (0.67 ± 0.01) V, a short-circuit current density (J_{sc}) of (0.30 ± 0.01) mA cm⁻², and a fill factor (FF) of $(56 \pm 2)\%$, whereas the superstructured solar cells perform slightly better with a PCE of $(0.13 \pm 0.01)\%$, a V_{oc} of (0.70 ± 0.01) V, a J_{sc} of (0.33 ± 0.01) mA cm⁻², and a FF of $(56 \pm 1)\%$. The better photovoltaic performance is ascribed to an enhancement in the V_{oc} and J_{sc} values. Furthermore, it is found that J_{sc} is approximately 10% higher for the superstructured solar cells than for the planar devices. This increment is in good agreement with light-absorption enhancement in the wet-imprinted active layer, which suggests that additional light scattering induced by the channeled superstructures mainly contributes to more charge-carrier generation and, therefore, the enhancement in J_{sc} .

The angular-dependent PCE and J_{sc} of both types of hybrid solar cells are displayed in Figure 6b,c. It is noticeable that the PCE and J_{sc} decrease gradually with increasing angles of light incidence. This trend is different from our previous observation in the hybrid solar cells with a square pitch-like lattice superstructure, which showed maximal PCE and J_{sc} values at a 5° incident angle.^[31] The decay in PCE over the investigated angular range mainly originates from the decrease in J_{sc} , as they have a similar trend. The light reflection at the glass substrate increases with the increasing angle of oblique incident light, whereby less light reaches the active layers and causes a decrease in J_{sc} . However, an improved J_{sc} value in the superstructured solar cells is found for all incident angles from 0 to 50° as compared to the planar devices. Moreover, the increased ratios of J_{sc} over

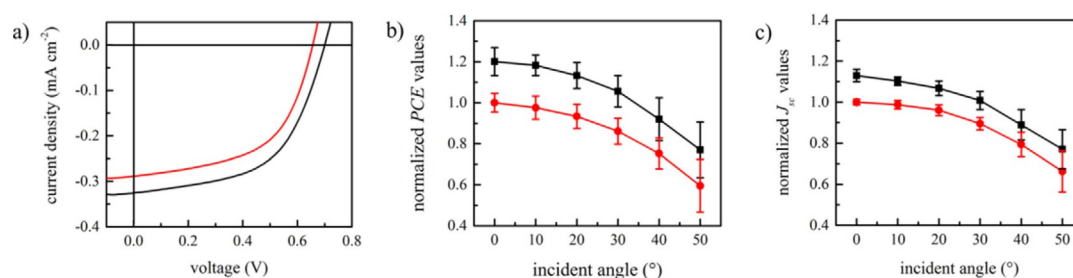


Figure 6. a) Example of J – V curves of wet-imprinted (black curve) and planar (red curve) dye-free hybrid solar cells measured at 0° of light incidence. Angular-dependent b) PCE and c) J_{sc} normalized to the planar solar cell measured at zero incident angle.

all investigated angles of light incidence are in line with the increased absorption ratios in the active layer, indicating that the enhanced J_{sc} value is caused by additional light absorption at all angles of light incidence. In contrast, the additional light scattering of the hierarchical titania structures does not influence the V_{oc} value or the FF, as their values are quite stable over all measuring angles (see Figure S2).

Conclusions

We demonstrated a low-temperature route for superimposing macroscopic 1D channeled superstructures on mesoporous titania films. Easy transfer of the superstructure from poly(dimethylsiloxane) molds was achieved by using a wet-imprinting process, which allowed for fabrication of hierarchically structured titania films over a large area with low costs and high throughput. Scanning electron microscopy and grazing incidence small-angle X-ray scattering measurements revealed the successful combination of channeled superstructures with a foam-like nanomorphology on titania films. The channels have an archy transverse section with a width of 0.80 μm , a height of 60 nm, and a periodicity of 1.35 μm , whereas the interconnected titania nanostructures have a pore size ranging from approximately 10 to 20 nm. Additional light-scattering abilities were found in the hierarchically structured titania films under various angles of light incidence. Moreover, an enhancement in light absorption was found in the superstructured active layer, which resulted in an improved short-circuit current density and thereby an enhanced power conversion efficiency in wet-imprinted hybrid solar cells over all investigated angles of light incidence without a particular angular dependence. Therewith, wet imprinting shows great potential for the fabrication of hierarchical structures for enhancing light harvesting, and it could be easily adapted to other thin-film photovoltaic systems such as colloidal nanocrystals, small-molecule organic semiconductors, and hybrid organic-inorganic perovskites.

Experimental Section

Chemicals

Polystyrene-block-polyethylene oxide [PS-*b*-PEO, $M_n(\text{PS}) = 20,500 \text{ g mol}^{-1}$, $M_n(\text{PEO}) = 8000 \text{ g mol}^{-1}$, polydispersity index, PDI = 1.02] was purchased from Polymer Source Inc., Canada. Ethylene-glycol-modified titanate (EGMT) was synthesized according to a reported method.^[60,61] *N,N*-Dimethylformamide (DMF, 99.8%) and HCl (12M) were purchased from Carl Roth GmbH, Germany. Silicone elastomer and curing agent of the Sylgard 184 were obtained from Sigma-Aldrich. Poly(3-hexylthiophene) (P3HT, $M_w = 53,000 \text{ g mol}^{-1}$, regioregularity = 92%, PDI = 2.3) was purchased from Rieke Metal Inc.. All chemicals were used as received without any further purification.

Fabrication of PDMS molds

Silicone-elastomer and curing agent were mixed together at a weight ratio of 10:1. After vigorous stirring, the mixture was put into a vacuum chamber to remove trapped air bubbles. Subsequently, the clear and viscous liquid was poured into square alumi-

num frames, which were placed on top of the pre-cleaned compact disc (CD) masters beforehand. The whole system comprising the CD substrates, aluminum frames, and PDMS solution was then put in a vacuum chamber for 2 min before annealing at 150 °C for 30 min to cure PDMS. Afterwards, the system was cooled to room temperature and the PDMS molds were peeled off and cut into the desired sizes. The obtained PDMS blocks were ultrasonicated in ethanol for 10 min to finalize the ready-to-use imprinting molds.

PS-*b*-PEO assisted sol-gel synthesis

The diblock copolymer PS-*b*-PEO was dissolved in DMF under vigorous stirring for 30 min. Subsequently, EGMT was mixed with HCl, and then the EGMT/HCl mixture was ultrasonicated for 10 min until the solution was clear. Afterwards, the EGMT solution was added dropwise into the polymer solution under constant stirring conditions. Then, the resulting mixture was stirred at 90 °C for 15 min prior to continuous stirring at 70 °C for 15 h. The weight ratio of the sol-gel components was kept constant at $W_{\text{DMF}}/W_{\text{HCl}}/W_{\text{EGMT}}/W_{\text{PS-}b\text{-PEO}} = 30:3:1:1$. After aging, the sol-gel solution was spin coated (2000 rpm, 30 s) to obtain titania:PS-*b*-PEO composite films, followed by an annealing process at 90 °C for 15 min. The spin-coating and annealing processes were repeated for a second time to increase the film thickness.

Wet imprinting and P3HT backfilling

The sol-gel solution (30 μL), which was used to produce the titania:PS-*b*-PEO composite films, was dropped on one edge of the PDMS mold before the spin-coated titania/PS-*b*-PEO composite film was placed on top. Subsequently, a 20 N force was applied on the backside of the film, followed by a drying process under ambient conditions. After 12 h of drying, the PDMS mold was lifted off. Then, the wet-imprinted composite film was exposed to UV irradiation for 20 h to remove the PS-*b*-PEO template. After removal of the polymer, the obtained hierarchically structured titania film was immersed in chlorobenzene for 40 min. This step was essential for P3HT backfilling. On the one hand, soaking of the sample in chlorobenzene helped to remove residual PS-*b*-PEO after UV extraction. On the other hand, chlorobenzene was the host solvent of the P3HT solution used for backfilling, and presoaking proved to increase the filling ratio of titania mesopores with P3HT.^[62] After the soaking process, the P3HT solution (15 mg mL^{-1} in chlorobenzene) was deposited onto the titania films by spin coating (900 rpm for 9 s, followed by 2500 rpm for 50 s) to finalize the active layer for hybrid solar cells.

Solar-cell fabrication

Fluorine-doped tin oxide (FTO)-coated glass substrates were etched with zinc powder and HCl to obtain the desired pattern. Then, the patterned substrates were consecutively cleaned with Alconox, ethanol, acetone, and isopropanol in an ultrasonic bath and finally by oxygen plasma for 10 min. Subsequently, a titania sol [titanium(IV) butoxide (850 μL), diethylamine (210 μL), and deionized H_2O (45 μL) in ethanol (3.88 mL)] was spin coated onto the pre-cleaned FTO substrates to form a compact titania layer. The detailed experimental procedure is described in the literature.^[63] Afterwards, the active layer was deposited onto the FTO/compact- TiO_2 substrates. To complete hybrid solar cells, gold electrodes were thermally evaporated on top of the active layer.

Film and device characterization

For optical microscopy, SEM, AFM, and GISAXS measurements, all investigated films were deposited on silicon substrates. Micrographs were taken with the aid of an Axiolab A microscope (Carl Zeiss). An NVision40 field emission scanning electron microscope (Carl Zeiss AG) with an accelerating voltage of 5 kV and a working distance of 3.0 mm was used for SEM measurements. AFM measurements were performed by using an Asylum MFP-3D instrument in tapping mode. GISAXS measurements were performed at the Austrian SAXS beamline of the Elettra synchrotron source in Trieste, Italy. The X-ray wavelength was $\lambda = 1.54 \text{ \AA}$ (energy of 8 keV). A grazing incident angle of 0.54° and a sample-to-detector distance of 1.73 m were selected to obtain a desirable q-range. During the measurements, the scattering signal was recorded by using a Pilatus3 1M detector that had a pixel size of $172 \mu\text{m} \times 172 \mu\text{m}$ and a 981×1043 pixel array. UV/Vis measurements were performed on the samples with glass substrates. The optical transmission of the active layers was measured by using a Lambda 35 UV/Vis spectrometer (PerkinElmer). *J-V* characteristics of the prepared hybrid solar cells were measured under ambient conditions by using a solar simulator Solar Constant1200 (K. H. Steuernagel Lichttechnik GmbH) with a simulated AM 1.5G solar illumination.

Acknowledgements

This work was supported by funding from TUM.solar in the context of the Bavarian Collaborative Research Project Solar Technologies Go Hybrid (SolTech), the Excellence Cluster Nanosystems Initiative Munich (NIM), the Center for NanoScience (CeNS), and the International Research Training Group 2022 Alberta/Technical University of Munich International Graduate School for Environmentally Responsible Functional Hybrid Materials (ATUMS). L.S. and W.W. acknowledge the China Scholarship Council (CSC); T.W. thanks the Erasmus Mundus MaMaSELF program; C.J.S. thanks the Bavarian State Ministry of Education, Science, and the Arts via the International Graduate School Materials Science of Complex Interfaces (Complnt); and V.K. thanks the Bavarian State Ministry of Sciences, Research, and Arts via the project Energy Valley Bavaria. The authors thank Prof. Alexander Holleitner and Peter Weiser for providing access to the scanning electron microscope.

Conflict of interest

The authors declare no conflict of interest.

Keywords: absorption • energy conversion • hierarchical structures • solar cells • light scattering

- [1] F. Gao, S. Ren, J. Wang, *Energy Environ. Sci.* **2013**, *6*, 2020–2040.
- [2] Y. Bai, I. Mora-Seró, F. D. Angelis, J. Bisquert, P. Wang, *Chem. Rev.* **2014**, *114*, 10095–10130.
- [3] S. S. Williams, M. J. Hampton, V. Gowrishankar, I.-K. Ding, J. L. Templeton, E. T. Samulski, J. M. DeSimone, M. D. McGehee, *Chem. Mater.* **2008**, *20*, 5229–5234.
- [4] C. Y. Kuo, W. C. Tang, C. Gau, T. F. Guo, D. Z. Jeng, *Appl. Phys. Lett.* **2008**, *93*, 033307.
- [5] D. Fattakhova-Rohlfing, A. Zaleska, T. Bein, *Chem. Rev.* **2014**, *114*, 9487–9558.

- [6] M. Rawolle, M. A. Niedermeier, G. Kaune, J. Perlich, P. Lellig, M. Memesa, Y. Cheng, J. S. Gutmann, P. Müller-Buschbaum, *Chem. Soc. Rev.* **2012**, *41*, 5131–5142.
- [7] L. Song, W. Wang, V. Körstgens, D. Moseguí González, F. C. Löhner, C. J. Schaffer, J. Schlipf, K. Peters, T. Bein, D. Fattakhova-Rohlfing, S. V. Roth, P. Müller-Buschbaum, *Nano Energy* **2017**, *40*, 317–326.
- [8] X. Fan, M. Zhang, X. Wang, F. Yang, X. Meng, *J. Mater. Chem. A* **2013**, *1*, 8694–8709.
- [9] R. A. Krüger, T. J. Gordon, T. Baumgartner, T. C. Sutherland, *ACS Appl. Mater. Interfaces* **2011**, *3*, 2031–2041.
- [10] J. Balko, R. H. Lohwasser, M. Sommer, M. Thelakkat, T. Thurn-Albrecht, *Macromolecules* **2013**, *46*, 9642–9651.
- [11] J.-F. Lin, W.-B. Wang, C.-C. Ho, J.-H. Jou, Y.-F. Chen, W.-F. Su, *J. Phys. Chem. C* **2012**, *116*, 1955–1960.
- [12] G. Mattioli, S. B. Dkhil, M. I. Saba, G. Mallocci, C. Melis, P. Alippi, F. Filippone, P. Giannozzi, A. K. Thakur, M. Gaceur, O. Margeat, A. K. Diallo, C. Vidolot-Ackermann, J. Ackermann, A. A. Bonapasta, A. Mattoni, *Adv. Energy Mater.* **2014**, *4*, 1301694.
- [13] S. Ben Dkhil, M. Gaceur, W. Dachraoui, D. Hannani, S. Fall, F. Brunel, M. Wang, G. Poize, J. Mawyin, I. Shupyk, C. Martini, E. Shilova, F. Fages, T. Ishwara, J. Nelson, T. Watanabe, N. Yoshimoto, O. Margeat, C. Vidolot-Ackermann, J. Ackermann, *Sol. Energy Mater. Sol. Cells* **2017**, *159*, 608–616.
- [14] M. A. Niedermeier, I. Groß, P. Müller-Buschbaum, *J. Mater. Chem. A* **2013**, *1*, 13399–13403.
- [15] T. P. Chou, Q. Zhang, G. E. Fryxell, G. Cao, *Adv. Mater.* **2007**, *19*, 2588–2592.
- [16] Y.-C. Shih, A.-K. Chu, W.-Y. Huang, *J. Nanosci. Nanotechnol.* **2012**, *12*, 3070–3076.
- [17] M. Aryal, K. Trivedi, W. Hu, *ACS Nano* **2009**, *3*, 3085–3090.
- [18] M.-S. Kim, J.-S. Kim, J. C. Cho, M. Shtein, L. J. Guo, J. Kim, *Appl. Phys. Lett.* **2007**, *90*, 123113–123115.
- [19] R. Meier, C. Birkenstock, C. M. Palumbiny, P. Müller-Buschbaum, *Phys. Chem. Chem. Phys.* **2012**, *14*, 15088–15098.
- [20] E. Kim, Y. Xia, G. M. Whitesides, *Nature* **1995**, *376*, 581–584.
- [21] Y. Xia, E. Kim, G. M. Whitesides, *Chem. Mater.* **1996**, *8*, 1558–1567.
- [22] P. Yang, T. Deng, D. Zhao, P. Feng, D. Pine, B. F. Chmelka, G. M. Whitesides, G. D. Stucky, *Science* **1998**, *282*, 2244–2246.
- [23] P. Yang, A. H. Rizvi, B. Messer, B. F. Chmelka, G. M. Whitesides, G. D. Stucky, *Adv. Mater.* **2001**, *13*, 427–431.
- [24] S. J. Clarson, J. A. Semlyen, *Siloxane Polymers*, Prentice Hall, Englewood Cliffs, NJ, **1993**.
- [25] A. Hagfeldt, G. Boschloo, L. Sun, L. Kloo, H. Pettersson, *Chem. Rev.* **2010**, *110*, 6595–6663.
- [26] J. Zhang, Y. Deng, D. Gu, S. Wang, L. She, R. Che, Z.-S. Wang, B. Tu, S. Xie, D. Zhao, *Adv. Energy Mater.* **2011**, *1*, 241–248.
- [27] L. Song, W. Wang, V. Körstgens, D. Moseguí González, Y. Yao, N. K. Minar, J. M. Feckl, K. Peters, T. Bein, D. Fattakhova-Rohlfing, G. Santoro, S. V. Roth, P. Müller-Buschbaum, *Adv. Funct. Mater.* **2016**, *26*, 1498–1506.
- [28] Y. J. Cheng, J. S. Gutmann, *J. Am. Chem. Soc.* **2006**, *128*, 4658–4674.
- [29] S. Guldin, M. Kolle, M. Stefik, R. Langford, D. Eder, U. Wiesner, U. Steiner, *Adv. Mater.* **2011**, *23*, 3664–3668.
- [30] H. Wang, C. C. Oey, A. B. Djurišić, M. H. Xie, Y. H. Leung, K. K. Y. Man, W. K. Chan, A. Pandey, J.-M. Nunz, P. C. Chui, *Appl. Phys. Lett.* **2005**, *87*, 023507.
- [31] L. Song, A. Abdelsamie, C. J. Schaffer, V. Körstgens, W. Wang, T. Wang, E. D. Indari, T. Fröschl, N. Hüsing, T. Haerberle, P. Lugli, S. Bernstorff, P. Müller-Buschbaum, *Adv. Funct. Mater.* **2016**, *26*, 7084–7093.
- [32] P. D. Cozzoli, A. Kornowski, H. Weller, *J. Am. Chem. Soc.* **2003**, *125*, 14539–14548.
- [33] P. Kohn, S. Pathak, M. Stefik, C. Ducati, U. Wiesner, U. Steiner, S. Guldin, *Nanoscale* **2013**, *5*, 10518–10524.
- [34] M. Rawolle, E. V. Braden, M. A. Niedermeier, D. Magerl, K. Sarkar, T. Fröschl, N. Hüsing, J. Perlich, P. Müller-Buschbaum, *ChemPhysChem* **2012**, *13*, 2412–2417.
- [35] L. Zhao, Y. Yu, L. Song, X. Hu, A. Larbot, *Appl. Surf. Sci.* **2005**, *239*, 285–291.
- [36] L. Song, W. Wang, S. Pröller, D. Moseguí González, J. Schlipf, C. J. Schaffer, K. Peters, E. M. Herzig, S. Bernstorff, T. Bein, D. Fattakhova-Rohlfing, P. Müller-Buschbaum, *ACS Energy Lett.* **2017**, *2*, 991–997.

- [37] W. Kim, S. Y. Choi, Y. M. Jeon, S.-k. Lee, S. H. Kim, *ACS Appl. Mater. Interfaces* **2014**, *6*, 11484–11492.
- [38] C. C. Oey, A. B. Djurišić, H. Wang, K. K. Y. Man, W. K. Chan, M. H. Xie, Y. H. Leung, A. Pandey, J.-M. Nunzi, P. C. Chui, *Nanotechnology* **2006**, *17*, 706–713.
- [39] J. Perlich, G. Kaune, M. Memesa, J. S. Gutmann, P. Müller-Buschbaum, *Philos. Trans. R. Soc. London Ser. A* **2009**, *367*, 1783–1798.
- [40] T. Fröschl, U. Hörmann, P. Kubiak, G. Kučerová, M. Pfanzelt, C. K. Weiss, R. J. Behm, N. Hüsing, U. Kaiser, K. Landfester, M. Wohlfahrt-Mehrens, *Chem. Soc. Rev.* **2012**, *41*, 5313–5360.
- [41] D. Wang, R. Yu, N. Kumada, N. Kinomura, *Chem. Mater.* **1999**, *11*, 2008–2012.
- [42] R. Rossmanith, C. K. Weiss, J. Geserick, N. Hüsing, U. Hörmann, U. Kaiser, K. Landfester, *Chem. Mater.* **2008**, *20*, 5768–5780.
- [43] Y. Denkwitz, M. Makosch, J. Geserick, U. Hörmann, S. Selve, U. Kaiser, N. Hüsing, R. J. Behm, *Appl. Catal. B* **2009**, *91*, 470–480.
- [44] K. M. Coakley, Y. Liu, M. D. McGehee, K. L. Frindell, G. D. Stucky, *Adv. Funct. Mater.* **2003**, *13*, 301–306.
- [45] M. C. Orilall, U. Wiesner, *Chem. Soc. Rev.* **2011**, *40*, 520–535.
- [46] X. Wang, J. C. Yu, C. Ho, Y. Hou, X. Fu, *Langmuir* **2005**, *21*, 2552–2559.
- [47] Y. Cai, H.-E. Wang, S.-Z. Huang, M. F. Yuen, H.-H. Cai, C. Wang, Y. Yu, Y. Li, W.-J. Zhang, B.-L. Su, *Electrochim. Acta* **2016**, *210*, 206–214.
- [48] K. Yin, Y. Cai, X. Zheng, Z. Deng, B.-L. Su, H.-E. Wang, *Mater. Lett.* **2017**, *201*, 93–96.
- [49] P. Müller-Buschbaum, *Adv. Mater.* **2014**, *26*, 7692–7709.
- [50] G. Renaud, R. Lazzari, F. Leroy, *Surf. Sci. Rep.* **2009**, *64*, 255–380.
- [51] W. Wang, C. J. Schaffer, L. Song, V. Körstgens, S. Pröller, E. Dwi Indari, T. Wang, A. Abdelsamie, S. Bernstorff, P. Müller-Buschbaum, *J. Mater. Chem. A* **2015**, *3*, 8324–8331.
- [52] Y. Yoneda, *Phys. Rev.* **1963**, *131*, 2010–2013.
- [53] M. Rauscher, R. Paniago, T. H. Metzger, Z. Kovats, J. Domke, J. Peisl, H.-D. Pfannes, J. Schulze, I. Eisele, *J. Appl. Phys.* **1999**, *86*, 6763–6769.
- [54] J. S. Pedersen, *J. Appl. Crystallogr.* **1994**, *27*, 595–608.
- [55] R. Hosemann, S. N. Bagchi, *Direct Analysis of Diffraction by Matter*, North-Holland Publishing, Amsterdam, **1962**.
- [56] R. Lazzari, *J. Appl. Crystallogr.* **2002**, *35*, 406–421.
- [57] M. Stefik, J. Song, H. Sai, S. Guldin, P. Boldrighini, M. C. Orilall, U. Steiner, S. M. Gruner, U. Wiesner, *J. Mater. Chem. A* **2015**, *3*, 11478–11492.
- [58] C. Karakaya, Y. Türker, Ö. Dag, *Adv. Funct. Mater.* **2013**, *23*, 4002–4010.
- [59] Z. S. Wang, H. Kawauchi, T. Kashima, H. Arakawa, *Coord. Chem. Rev.* **2004**, *248*, 1381–1389.
- [60] X. Jiang, T. Herricks, Y. Xia, *Adv. Mater.* **2003**, *15*, 1205–1209.
- [61] X. Jiang, Y. Wang, T. Herricks, Y. Xia, *J. Mater. Chem.* **2004**, *14*, 695–703.
- [62] M. Rawolle, K. Sarkar, M. A. Niedermeier, M. Schindler, P. Lellig, J. S. Gutmann, J.-F. Moulin, M. Haese-Seiller, A. S. Wochnik, C. Scheu, P. Müller-Buschbaum, *ACS Appl. Mater. Interfaces* **2013**, *5*, 719–729.
- [63] H. Yu, S. Zhang, H. Zhao, G. Will, P. Liu, *Electrochim. Acta* **2009**, *54*, 1319–1324.

 Manuscript received: January 19, 2018

Accepted manuscript online: February 14, 2018

Version of record online: March 15, 2018